Università degli studi di Udine

Polarization switching and AC small-signal capacitance in Ferroelectric Tunnel Junctions

(Article begins on next page)

14 July 2024

Polarization switching and AC small–signal capacitance in Ferroelectric Tunnel Junctions

M. Segatto[1,†], M. Massarotto[1,†], S. Lancaster[2], Q. T. Duong[2], A. Affanni[1], R. Fontanini[1], F. Driussi[1], D. Lizzit[1], T. Mikolajick[2,3], S. Slesazeck[2], D. Esseni[1]

[1]DPIA, University of Udine, Udine, Italy; [2]NaMLab gGmbH, Dresden, Germany;

[3]Chair of Nanoelectronics, IHM, TU–Dresden, Germany.

[†]These authors have equally contributed to the work.

Abstract

We here report a joint experimental and simulation analysis for large signal P-V and AC small–signal C-V curves in ferroelectric tunnel junctions. The attempt to reproduce both experimental data sets with the same model and material parameters challenges our understanding of the underlying physics, but it also helps develop a sound background for the device design.

I. Introduction

Memories and memristors based on ferroelectric $Hf(Zr)O_2$ have recently emerged as competitive options for conventional and novel neuromorphic hardware [1]. In Ferroelectric Tunnel Junctions (FTJs) the tunnelling barrier is altered by the ferroelectric polarization state [2], whereas in ferroelectric field–effect transistors (FeFETs) the polarization affects the threshold voltage and the read current of the FeFET [3], [4]. The polarization P at the interface between the ferroelectric and a thin dielectric layer governs the operation of both devices.

Experimental characterization and sound modelling are both paramount for an optimal design of ferroelectric devices. The multi–domain Landau, Ginzburg, Devonshire (LGD) theory is well credited for the ferroelectric dynamics, and it has been used for negative capacitance effects [5]–[9], as well as for the operation of FTJs [10] and of FeFETs [11]. The most appropriate thermodynamic potential in the presence of free charges in the dielectric stack has been recently revisited in [12].

This paper presents an investigation of the AC small–signal C–V curves (SSCV) in metal–ferroelectric–dielectric–metal (MFDM) FTJs (Fig. 1), whereby measurements are obtained with a purposely developed experimental setup, and simulations with a rigorous linearization of the LGD model. An instructive insight
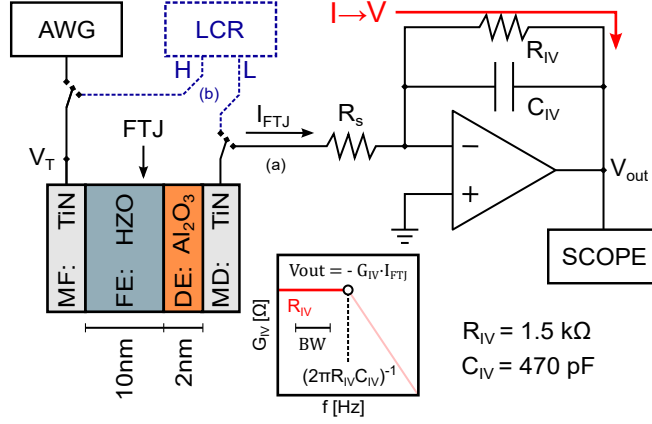
Figure 1: Sketch of the MFDM FTJs of this work and of the experimental setup. The setup consists of two distinct parts: (a) Virtual–grounded I→V converter (R_{IV}=1.5 kΩ, C_{IV}=470 pF) to measure the switching current I_{FTJ} through an oscilloscope. The inset shows the bandwidth (BW) of the amplifier; (b) An LCR meter to measure the AC small–signal capacitance.

is reported by comparing simulations and experiments for both the large–signal P–V curves (LSPV) and the SSCV response.

II. Device fabrication

The MFDM FTJ structure consists of $\approx$10 nm Hf$_{0.5}$Zr$_{0.5}$O$_2$ (HZO) and $\approx$2 nm Al$_2$O$_3$ deposited via ALD on top of a W (30 nm)/TiN (10 nm) electrode. The 10 nm TiN top electrode was also deposited via sputtering under ultra–high vacuum. The HZO was crystallized by annealing at 500 °C for 20 s. Finally, capacitor structures were formed by depositing 10 nm Ti/25 nm Pt through a shadow mask and etching the TiN layer. For both electrodes, UHV sputtering ensures a low resistivity of around $3 \cdot 10^{-6}$ Ω m so that the voltage is dropped mainly over the active bilayer. The Al$_2$O$_3$ tunneling layer in series with the ferroelectric increases the coercive voltage V_c of the stack to $\approx \pm 2$ V. More switching properties of these devices have been reported elsewhere [13].

III. Experimental setup and results

Triangular pulses with an amplitude of several Volts are typically used to measure LSPV curves, while an AC small-signal is used for SSCV measurements. It has been argued that the irreversible polarization switching dominates LSPV measurements, while it gives a negligible contribution to SSCV curves [14], [15]. In order to directly inspect the current response to the AC small-voltage in an FTJ, we developed the experimental setup of Fig. 1. An arbitrary waveform generator (AWG, Agilent 33250A) supplies V_T at the MF metal electrode, while the current I_{FTJ} is measured at the virtual–grounded MD metal contact through an I→V converter [13]. The OPAMP (TI TL082CP) feedback loop defines the trans–impedance of the amplifier (V_{out}=$-R_{IV}I_{FTJ}$) inside its bandwidth BW=$(2\pi R_{IV}C_{IV})^{-1}$. The V_{out} is finally monitored through an oscilloscope (Tektronix TDS520B). This versatile setup allows us to measure the P–V curves using triangular pulses, as well as the AC small–signal response to a sinusoidal input. Moreover, we also measured SSCV curves by using an LCR meter (HP 4284A).
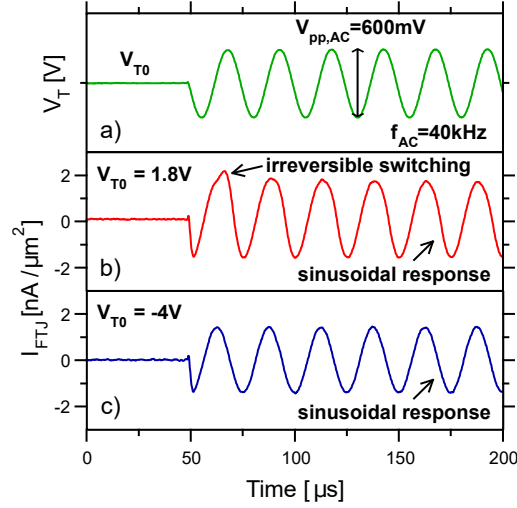
Figure 2: Emulation of an AC measurement by using the I→V converter. (a) Sinusoidal V_T waveform superimposed to a DC bias V_{T0}. (b) Measured I_{FTJ} for V_{T0}=1.8 V which is close to the positive coercive voltage of the FTJ (see Fig. 4a). A deviation of the I_{FTJ} from the sinusoidal waveform is observed during the first positive half–period, which we ascribe to irreversible polarization switching.

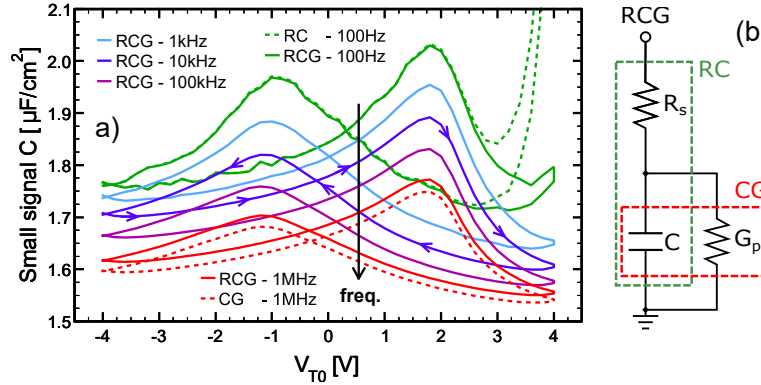(c) I_{FTJ} for V_{T0}=−4 V showing a sinusoidal–only response.

Figure 3: (a) SSCV curves measured with the LCR meter in the 100 Hz–1 MHz range and according to the different equivalent circuits sketched in (b), namely the RC series (green, dashed), the CG parallel (red, dashed) and the hybrid series–parallel RCG (solid line) circuit.

As shown in Fig. 2, we used the AWG to emulate the V_T waveform used in LCR based measurements, and recorded the current for different DC bias values V_{T0}. Figure 2 shows that an evidence of irreversible switching is observed only during the first positive AC semi–period at V_{T0}=1.8 V, which is close to the positive coercive voltage (see Fig. 4a). The I_{FTJ} is instead clearly sinusoidal in the following periods, despite the relatively large 300 mV amplitude of the AC signal. The analysis in Fig. 2 excludes that a non–linear I_{FTJ} response to the AC V_T waveform can affect the SSCV curves detected by an LCR meter.

Figure 3a shows the hysteretic butterfly–shaped C–V curves measured with an LCR meter at different AC frequencies f ranging from 100 Hz to 1 MHz. The reasonably bias–independent capacitance measured at

$V_{T0} \approx \pm 4\,\text{V}$ is quite close to the estimated series capacitance $C_s = 1.44\,\mu\text{F cm}^{-2}$ due to the sole linear dielectric response of the FTJ stack (for $\varepsilon_{FE} = 30$, $\varepsilon_{DE} = 9$). Since the frequency dependence in Fig. 3a may be affected by the capacitance extraction method, we compared the results for different equivalent circuits (see Fig. 3b). Solid lines in Fig. 3a were obtained with a hybrid series–parallel RCG circuit, whereby the R_s at each V_{T0} was estimated as the real part of the impedance at $1\,\text{MHz}$ (assuming that at $1\,\text{MHz}$ the influence of leakage through the FTJ is negligible). As expected, the series RC model (green, dashed) deviates from the RCG results at small f and large V_{T0} because it misrepresents the leakage. The accuracy of the parallel CG scheme (red, dashed), instead, degrades at high frequency because it cannot capture the influence of R_s. The experimental data compared with simulations have always been extracted with the RCG model.

IV. Simulation methods and results

The SSCV curves in ferroelectric materials and devices have been investigated to a lesser extent compared to the LSPV counterpart. In particular, it is unclear if the same model and material parameters explaining a given set of P–V curves can reproduce equally well the corresponding SSCV curves. There is, however, a consensus that LSPVs measure the irreversible polarization switching, while the SSCVs mainly probe a reversible component, typically interpreted as a domain wall motion (DWM) [15]. In this latter respect, it has been argued that the DWM effects are adequately represented in the LGD equations [16], [17], thus even in their small–signal linearization.

Our modeling methodology solves the multi-domain LGD equations, that for n_D domains read [7], [8]

$$
\begin{aligned}
\frac{\partial P}{\partial t} = \frac{1}{t_F\,\rho} \Big[&- \left(2\alpha_i\,P_i + 4\beta_i\,P_i^3 + 6\gamma_i\,P_i^5\right) t_F + \\
&- \frac{t_F\,k}{d\,w} \sum_n (P_i - P_n) + \\
&- \frac{1}{2} \sum_{j=1}^{n_D} \left(\frac{1}{C_{i,j}} + \frac{1}{C_{j,i}}\right)(P_j + Q_{Tj}) + \frac{C_D}{C_0} V_T \Big]
\end{aligned}
\tag{1}
$$

where P_i, Q_{Ti} are the polarization and trapped charge in domain i, and the sum over n is restricted to the domains sharing a domain wall with domain i. Moreover, α_i, β_i, γ_i are the anisotropy constants, ρ is a switching resistivity, d is the side of square domains, k and w are respectively the domain wall coupling coefficient and wall width, and $C_{i,j}$ are capacitive couplings between domains [7].

The ferroelectric dynamics is self-consistently solved with first order dynamic equations for traps at the FE-DE interface. Traps are assumed to exchange charge only with the MD electrode (in virtue of the much thicker ferroelectric layer) and the dynamic equations read [7]:

$$
\frac{\partial n_{tr,i}(E_T)}{\partial t} = c_n\left[N_T - n_{tr,i}\right] - e_n n_{tr,i}
\tag{2}
$$

where $n_{tr,i}(E_T)$ is the density of trapped electrons at energy E_T in domain i, while N_T is the corresponding trap density. The $c_n(E_T)$ and $e_n(E_T)$ denote the capture and emission rates with $e_n = e_{n0}\,F_0[(E_{f,MD} - E_T)/K_B T]$, where e_{n0} is a bias independent rate, $F_0(\eta)$ is the Fermi-Dirac function and $E_{f,MD}$ the Fermi level at the MD

electrode.[1] The c_n is linked to e_n by $c_n = e_n \exp[(E_{f,MD} - E_{Tr})/K_B T]$, which ensures that the steady-state occupation of traps deriving from Eq. 2 is in thermodynamic equilibrium with $E_{f,MD}$. A set of Eqs. 2 is solved for both donor and acceptor type traps, and the overall trapped charge Q_{Ti} in each domain is $Q_{Ti} = Q_{Ti,acc} + Q_{Ti,don}$.

Figure 4a reports the experimental $P-V$ curves corresponding to triangular pulses at a frequency $f=1\,\text{kHz}$, and Fig. 4b shows also an effective large-signal capacitance curve (LSCV), that was extracted by dividing the current during the triangular pulse by the slope of the voltage ramp, namely as $\text{LSCV} = I_{FTJ}/(dV_T/dt)$. Figure 4b confirms that the measured LSCV curves are much larger than the SSCV counterparts (see Fig. 3a), due to the irreversible switching component.

Figures 4a and 4b also report the simulated LSPV and LSCV curves. In simulations we used nominal values of anisotropy constants α, β and γ equal to respectively $-3.8 \cdot 10^8$ m/F, $-3.2 \cdot 10^{10}$ m^5/(FC^2) and $7.9 \cdot 10^{11}$ m^9/(FC^4), and then introduced a domain to domain fluctuations of α, β, γ corresponding to a standard deviation $\sigma_{Ec}=30\%$ of the coercive field (normalized to mean value). Simulations assume a fully ferroelectric HZO film (i.e. 100% orthorhombic phase), unless otherwise stated. The switching resistivity was set to $\rho=110\,\Omega\,\text{m}$ [18], while the domain wall coupling k was set to zero, if not otherwise stated, by following recent first principle calculations for HfO$_2$ [19]. Figure 4a shows that simulations neglecting any trapping at the FE-DE interface result in much narrower and more tilted curves compared to experiments. We have already emphasized this behavior in [20], and discussed the links to the previous literature [21]. Only a fairly large density of traps at the FE-DE interface can reconcile simulations with experiments, and our trap densities are consistent with values extracted in [22], [23]. Even for the LSCV curves the simulations neglecting trapping show a large discrepancy with experiments, whereas the agreement improves drastically by including traps.

As for the simulation of the AC small–signal response, we note that Eqs. 1 and 2 can be collectively denoted as

$$\frac{\partial Y_h}{\partial t} = F_h(Y_h, V_T(t)) \tag{3}$$

where Y_h is a generic unknown (i.e. P_i or $n_{tr,i}(E_T)$), with $h=1, 2, \cdots N_{PT}$ and N_{PT} being the number of equations. With a standard notation, the AC small–signal version of Eq. 3 at the radial frequency ω can be written as:

$$j\omega \widetilde{Y_h} = \sum_{k=1}^{N_{PT}} J_{h,k} \widetilde{Y_k} + \left.\frac{\partial f_h}{\partial V_T}\right|_{V_{T,0}} \widetilde{V_T} \tag{4}$$

where $J_{h,k}$ is an entry of the Jacobian matrix $J_{hk} = \partial F_h/\partial Y_k$, while $\widetilde{V_T}$ is the AC external bias. Equation 4 is a linear problem for the unknowns $\widetilde{Y_h}$, from which the AC- small–signal terminal currents and thus the small–signal capacitance can be readily calculated.

Figure 5 compares the experimental SSCV with simulations at an AC frequency $f=100$ kHz. The simulations without traps do not show the capacitance peaks at the coercive V_T voltages observed in experiments.

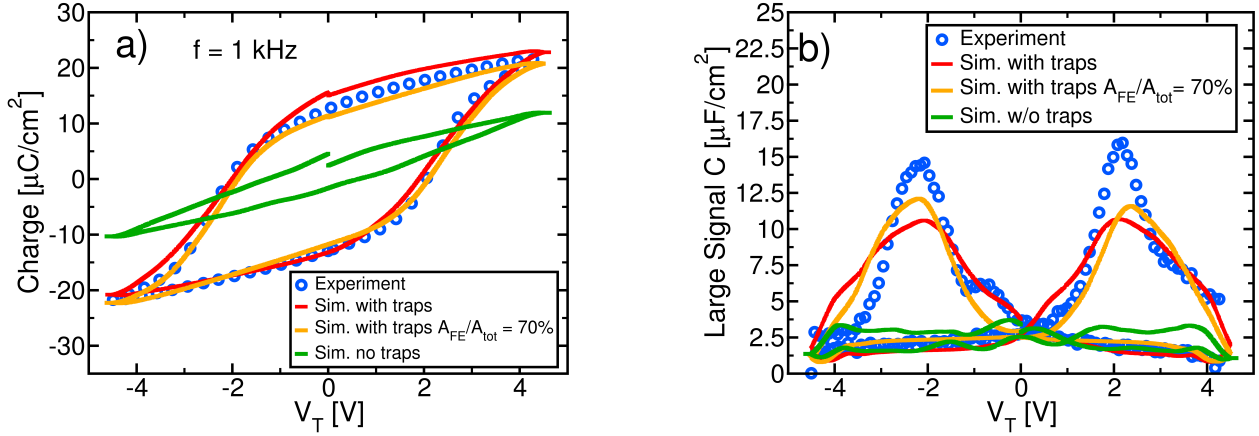[1] The Fermi-Dirac occupation function $F_0(\eta)$ is defined as $F_0(\eta)=1/[1 + \exp(\eta)]$.

Figure 4: Comparison of measured (symbols) and simulated (lines) LSPV curves (a), and LSCV curves (b), for an Al_2O_3 thickness $t_{DE} = 2\,nm$. Simulations are shown for no trapped charge (green line), and for a density of acceptor and donor type traps equal to respectively $N_{acc}=4.7 \cdot 10^{13}\,cm^{-2}\,eV^{-1}$ and $N_{acc}=5.4 \cdot 10^{13}\,cm^{-2}\,eV^{-1}$ and over a $2.5\,eV$ energy range. Simulations for a 70% ferroelectric area in the HZO film (i.e. $A_{FE}/A_{tot}=70\%$) are also reported for $N_{acc}=5.9\cdot 10^{13}\,cm^{-2}\,eV^{-1}$ and $N_{don}=9.6 \cdot 10^{13}\,cm^{-2}\,eV^{-1}$. The bias-independent trapping emission rate in Eq.2 is $e_{n0} = 2 \cdot 10^4\,s^{-1}$.
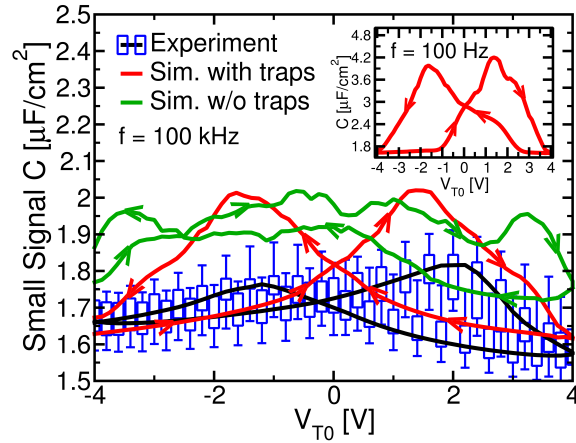

Figure 5: Measured (box plot, blue) and simulated (lines) small–signal capacitance curves at an AC frequency f=100 kHz and for the same device as in Fig. 4a. Measurements correspond to ten nominally identical devices. Simulations with and without trapping are displayed. The inset shows simulations at f=100 Hz.

Simulations with traps reproduce quite well the capacitance at large $|V_T|$ values and the coercive voltages, but they overestimate the measured peak capacitance. At lower frequencies the discrepancy with experiments gets worse (see inset), because the simulated capacitance enlarges significantly due to AC response of traps (which is negligible at f=100 kHz), whereas the increase in experiments is comparatively much smaller (see also Fig. 3a). This mismatch may hint that traps are located deeper inside the ferroelectric bulk and have longer time constants compared to simulations.

Figure 6a illustrates the effect of a non negligible domain wall coupling k, which is expected to enhance the capacitance contribution due to domain wall motion. Larger k values emphasize the discrepancy with

experiments in the peak capacitance region, besides being in contrast with first principle calculations [19].

We now recall that in our HZO films the fraction of orthorhombic ferroelectric phase can reasonably vary between 50% to 70% [24]. Figures 4a and 4b reveal that simulations with 70% ferroelectric area (i.e. A_{FE}/A_{tot}=70%) can still reproduce well the experimental LSPV and LSCV curves by adjusting the trap densities. Moreover Fig. 6b shows that, by accounting for a non ferroelectric area in the HZO film, the simulated peak capacitance in SSCV curves is reduced (for fixed values of the LGD anisotropy constants), thus improving the agreement with experiments, particularly for the positive V_T values.
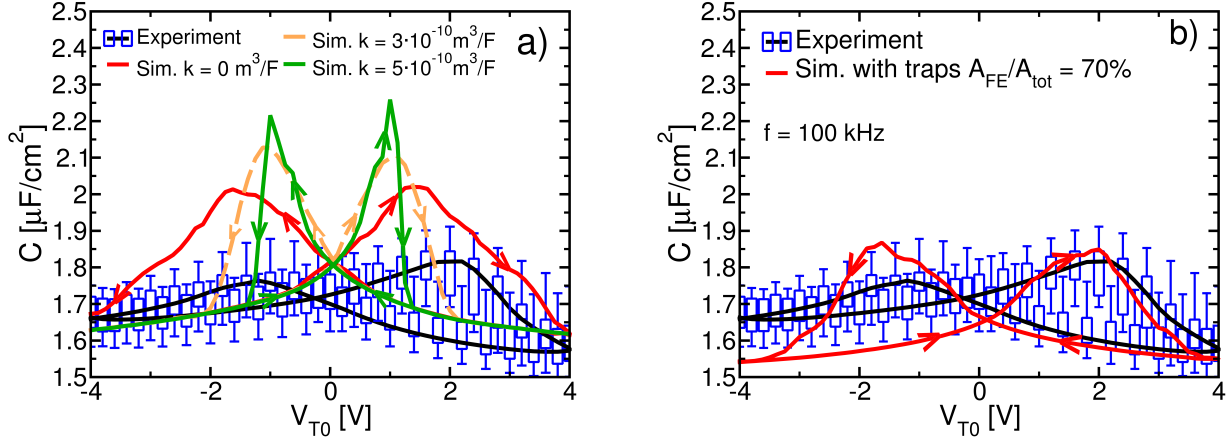

Figure 6: Measured and simulated capacitance as in Fig. 5 but for: (a) different values of the domain wall coupling k; (b) 70% fraction of ferroelectric over total area. The AC frequency is f=100 kHz.

V. CONCLUSIONS

We have reported experimental characterization and numerical modelling for LSPV and SSCV curves of MFDM based FTJs. As already pointed out in [20], our simulations can be reconciled with experiments only by accounting for charge trapping at the FE-DE interface. In our simulations the AC response of spontaneous polarization is not due to domain wall motion, in fact the domain wall coupling k was set to zero, and an increase of k impairs the agreement with experiments. By duly accounting for a fraction of non ferroelectric domains in the HZO film, the agreement with expriments of simulated SSCV curves is improved.

REFERENCES

[1] S. Slesazeck and T. Mikolajick, "Nanoscale resistive switching memory devices: a review", Nanotech., vol. 30, p. 352003, 2019.

[2] B. Max *et al.*, "Direct correlation of ferroelectric properties and memory characteristics in Ferroelectric Tunnel Junctions", IEEE JEDS, vol. 7, pp. 1175-1181, 2019.

[3] M. Jerry *et al.*, "Ferroelectric FET analog synapse for acceleration of deep neural network training" IEEE IEDM, 2017, pp. 6.2.1-6.2.4.

[4] H. Mulaosmanovic *et al.*, "Investigation of accumulative switching in Ferroelectric FETs: Enabling universal modeling of the switching behavior" IEEE TED, vol. 67, p. 5804, 2020.

[5] M. Hoffmann *et al.*, "On the stabilization of ferroelectric negative capacitance in nanoscale devices", Nanoscale, vol. 10, pp. 10891–10899, 2018.

[6] P. Lenarczyk and M. Luisier, "Physical modeling of ferroelectric field-effect transistors in the negative capacitance regime", IEEE SISPAD, pp. 311-314, 2016.

[7] T. Rollo *et al.*, "Stabilization of negative capacitance in ferroelectric capacitors with and without a metal interlayer", Nanoscale, vol. 12,, pp. 6121–6129, 2020.

[8] D. Esseni and R. Fontanini, "Macroscopic and microscopic picture of negative capacitance operation in ferroelectric capacitors", Nanoscale, vol. 13, pp. 9641–9650, 2021.

[9] M. Hoffmann *et al.*, "Intrinsic nature of negative capacitance in multidomain $Hf_{0.5}Zr_{0.5}O_2$-based ferroelectric/dielectric heterostructures", Adv. Funct. Mater., vol. 32, p. 2108494, 2022.

[10] Z. Zhou *et al.*, "Time-dependent Landau-Ginzburg equation-based Ferroelectric Tunnel Junction modeling with dynamic response and multi-domain characteristics", in IEEE EDL, vol. 43, no. 1, pp. 158-161, 2022.

[11] Y. Liu *et al.*, "Investigation of the impact of externally applied out-of-plane stress on Ferroelectric FET," IEEE EDL, vol. 42, no. 2, pp. 264-267, 2021.

[12] J. Bizindavyi *et al.*, "Thermodynamic equilibrium theory revealing increased hysteresis in ferroelectric field-effect transistors with free charge accumulation", Communic. Physics, 4:86, 2021.

[13] M. Massarotto *et al.*, "Versatile experimental setup for FTJ characterization", accepted for presentation at EuroSOI-ULIS 2022.

[14] Y. Qu *et al.*, "Quantitative characterization of interface traps in ferroelectric/dielectric stack using conductance method", IEEE TED, vol. 67, pp. 5315–21, 2020.

[15] S. Deng *et al.*, "Examination of the interplay between polarization switching and charge trapping in Ferroelectric FET", IEEE IEDM, pp. 4.4.1-4.4.4, 2020.

[16] P. Marton *et al.*, "Domain walls of ferroelectric $BaTiO_3$ within the Ginzburg-Landau-Devonshire phenomenological model", Phys. Rev. B, vol. 81, p. 144125, 2010.

[17] A. K. Saha *et al.*, "Phase field modeling of domain dynamics and polarization accumulation in ferroelectric HZO", Applied Physics Letters, vol. 114, p. 202903, 2019.

[18] M. Kobayashi *et al.*, "Experimental study on polarization-limited operation speed of Negative Capacitance FET with ferroelectric HfO_2", IEEE IEDM, pp. 12.3.1-12.3.4, 2016.

[19] H. J. Lee *et al.*, "Scale-free ferroelectricity induced by flat phonon bands in HfO_2", Science, vol. 369, no. 6509, p. 1343–1347, 2020.

[20] R.Fontanini *et al.*, "Polarization switching and interface charges in BEOL compatible Ferroelectric Tunnel Junctions", IEEE ESSDERC, no. 51, pp. 255-258, 2021.

[21] H. W. Park *et al.*, "Polarizing and depolarizing charge injection through a thin dielectric layer in a ferroelectric–dielectric bilayer", Nanoscale, vol. 13, pp. 2556–2572, 2021.

[22] K. Toprasertpong *et al.*, "Direct observation of interface charge behaviors in FeFET by quasi-static Split C-V and Hall techniques: Revealing FeFET operation", IEEE IEDM, pp. 23.7.1-23.7.4, 2019 methods", IEEE VLSI, pp. 1–2, 2020.

[23] S. Zhao *et al.*, "Experimental extraction and simulation of charge trapping during endurance of FeFET with TiN/HfZrO/SiO2/Si (MFIS) gate structure", IEEE TED, vol. 69, no. 3, pp. 1561-1567, 2022.

[24] U. Schroeder *et al.*, "Recent progress for obtaining the ferroelectric phase in hafnium oxide based films: impact of oxygen and zirconium", Jap. Journal of Appl. Phys., vol. 58, p. SL0801, 2019.